

1 **Assessing human appropriation of net primary production in various vegetation types based**
2 **on the spatio-temporal fusion model in Xiong'an New Area during 2000-2018**

3 Jia Tang¹, Qing Zhang², Jingyu Zeng¹, Rongrong Zhang¹, Xingrong Li², Yanqin Tian², Qianfeng
4 Wang^{1,3,*}

5 **Abstract**

6 **Background:** Humans have induced great changes in terrestrial ecosystems. The
7 human appropriation of net primary production (HANPP) quantifying the intensity of
8 anthropogenic extraction from ecosystem has been widely used to evaluate ecological
9 sustainable development. However, the coarse-resolution of calculating data for the
10 HANPP leads to biased results in a small scale. Furthermore, the spatio-temporal
11 patterns and dynamics of the HANPP in a human-dominated heterogeneous region are
12 still unclear.

13 **Methods:** This study investigates the state-level new area Xiong'an New Area and
14 applies the spatial and temporal nonlocal filter-based fusion model (STNLFFM) to
15 generated new datasets, which is combined with our previously improved Carnegie–
16 Ames–Stanford approach (CASA) to estimate HANPP. Spatio-temporal variations of
17 HANPP are mapped and assessed using Mann–Kendall (M–K) trend analysis approach
18 from 2000 to 2018 with a high resolution. The relationship among the HANPP,
19 subcomponents, and natural–social–economic-driven factors is discussed herein.

* Correspondence: Qianfeng Wang, College of Environment and resource, Fuzhou University, Fuzhou,
China. Tel.: +86 131 2317 4301; fax: +86 59122866077; E-mail: wangqianfeng@fzu.edu.cn

20 **Results:** The results show that the STNLFFM-derived fusion images fitted well with
21 the observed images having the superior correlation coefficient (r), structural similarity
22 index, root mean square error, and mean absolute deviation of 0.75, 0.76, 0.035, and
23 0.026, respectively, and the normalized difference vegetation index (NDVI) differences
24 are mainly concentrated on the range of 0–0.15 for all months. The HANPP derived by
25 the fusion-based images, above 60% of potential NPP, varied across the whole area,
26 especially between various vegetation types. The HANPP exhibited a significant
27 positive correlation ($r > 0.46$, $P < 0.05$) with precipitation and held an uptrend because
28 of the increase of the harvested HANPP which related with the socio-economic
29 conditions having the determination coefficients above 0.76.

30 **Conclusions:** The spatio-temporal fusion contributed to fine spatial patterns and trends
31 of HANPP among various vegetation types. Though the harvested HANPP increased
32 from 2000 to 2018, the agricultural and socio-economic developments did not bring
33 extensive HANPP growth, indicating that the expansion has not violated its sustainable
34 development goal. The results provide a deep insight of the background characteristics
35 in Xiong'an New Area, which has great potential in supporting the future scientific
36 construction of the new area.

37 **Keywords:** Spatio-temporal fusion; Mann–Kendall trend analysis; Human
38 appropriation of net primary production; Dynamic; Driven factors

39 **Background**

40 The resources necessary for human development mainly come from the vegetation
41 products or materials in terrestrial ecosystems ([Huang et al. 2020](#)). Accompanied with

42 population growth and urbanization, humans have induced great changes in terrestrial
43 ecosystems, which constantly approached upper limits for the terrestrial ecosystems
44 (Running 2012). Over the past 50 years, global agricultural and forestry productions
45 have increased by 30% and 200%, respectively (Godfray et al. 2010; Warman 2014).
46 By 2011, at least 29% of the Earth's surface had been converted into a high-density
47 built-up area, or a high-intensity agricultural land (Ellis 2011). Moreover, global
48 population will reach 9.7 billion, with the urban population accounting for 69%, in the
49 next 30 years, which is expected to lead to a further expansion of 10^9 ha of agricultural
50 lands (Zhou et al. 2018). Therefore, the anthropogenic appropriation from terrestrial
51 ecosystems must be precisely monitored to realize the sustainable development goals
52 (SDG). The human appropriation of net primary production (HANPP) is a
53 comprehensive socioecological indicator coupling human extraction from various
54 vegetation types, which has attracted extensive attention and become one of the widely
55 used methods for assessing sustainable development (Krausmann et al. 2013).

56 Net primary production (NPP) is the key subcomponent of HANPP that refers to
57 the fixed net carbon amount of vegetation per unit area after photosynthesis
58 accumulation and respiration consumption in a certain period (Artacho and Bonomelli
59 2017). NPP is a critical, but limiting natural resource that supports all heterotrophs,
60 including humans (Zhang et al. 2018). Many methods had been developed to simulate
61 both the potential and the actual NPPs in terrestrial ecosystem (Huang et al. 2020). For
62 example, the Miami empirical model (Lieth 1975), light use efficiency-based model
63 (Haberl 1997), and vegetation physiological dynamics process-based model (Haberl et

64 [al. 2007](#)), had all been applied for potential NPP estimation. Meanwhile, the Lund–
65 Potsdam–Jena method ([Haberl et al. 2007](#)), Carnegie–Ames–Stanford approach
66 (CASA) ([Zhu et al. 2007](#)), and mixed approach ([Fetzel et al. 2014](#)), had all been used
67 for the actual NPP simulation. Among these models, the CASA based on remote sensing
68 data showed good efficiency on both potential and actual NPP simulations in a regional
69 scale ([Pachavo and Murwira 2014](#)). Our previous study improved the CASA model to
70 simulate the NPP in China during the early 21st century by considering land cover
71 change ([Wang et al. 2018](#)).

72 Spatio-temporal fusion model of remote sensing can provide a cost-effective
73 method for retrieving the NPP across spatio-temporal scales with a fine-resolution
74 ([Tang et al. 2020a](#)). As most of remote sensing data are either only available on higher
75 spatial resolution or higher temporal resolution, the compromises between the spatial
76 and temporal resolutions limit detailed, fine-scale accounts of NPP spatial patterns and
77 its dynamics ([Tang et al. 2020b](#)). Spatio-temporal fusion model can cope with these
78 resolution tradeoffs by combining the advantages of multi-source remote sensing
79 images and has been developed in heterogeneous regions ([Zhu et al. 2010](#); [Zhu et al.](#)
80 [2016](#); [Cheng et al. 2017](#); [Tang et al. 2020a](#)). Fusion images with both high spatial and
81 temporal resolutions have been successfully applied in agriculture production
82 estimation ([Liao et al. 2019](#)), forest disturbance monitoring ([Schmidt et al. 2015](#)) and
83 urban expansion surveying ([Nduati et al. 2019](#)). However, studies integrating the fusion
84 model into NPP simulation in regional scale are still lacking. Therefore, it is necessary

85 to use the fusion model to sufficiently mine information on remote sensing images and
86 then provide fine datasets for NPP simulation.

87 HANPP, which is defined as the sum of the NPP harvested via human productive
88 activities and the NPP changed by human-dominated land use conversion ([Haberl et al.
89 2014](#)), has been increasingly used to measure the extent of human domination and
90 transformation of ecosystems ([Haberl et al. 2007](#)). Quantifying HANPP can facilitate
91 the understanding of carbon cycling, ecosystem services, and sustainable development,
92 which has triggered considerable attention among global scholars ([Huang et al. 2018](#)).
93 Previous studies concentrated more on large spatial scales such as global scale ([Haberl
94 et al. 2007](#); [Krausmann et al. 2013](#); [Zhou et al. 2018](#)), continental scale ([Fetzel et al.
95 2016](#); [Plutzer et al. 2016](#)) and national scale ([Fetzel et al. 2014](#); [Niedertscheider and
96 Erb 2014](#); [Niedertscheider et al. 2014](#)), while fewer studies have focused on the regional
97 scale ([Andersen et al. 2015](#)). However, because of the regional heterogeneity, even the
98 same intensity of human activities can cause various extents of the HANPP in different
99 regions ([Zhang et al. 2018](#)). Furthermore, limited by the coarse resolution of calculating
100 data for HANPP, the detailed analysis of HANPP dynamics in a heterogeneous region
101 has not yet been clearly understood. Fine resolution HANPP in a human-dominated
102 heterogeneous region, however, would provide precise spatio-temporal information for
103 the deep evaluation of the region-specific ecological effect (e.g., sustainability),
104 mastering the driven factors and clarifying the impacts of policy making ([Erb 2012](#)).
105 Therefore, research should be more detailed and refined on specific region.

106 Xiong'an New Area is a state-level new area in China that serves to phase out the
107 non-capital functions from Beijing, explore a new model of optimized development in
108 densely populated areas, and restructure the urban layout in the Beijing, Tianjin, and
109 Hebei (BTH) region. As the deputy capital of China, eco-environmental protection and
110 green ecological development in this area are the top priorities (Song et al. 2018).
111 However, the construction of a new area may bring several ecological risks, including
112 reduction of biodiversity, shortage of water resources, and degradation of the ecosystem
113 health (Xu et al. 2013; Song et al. 2018; Xie et al. 2019). Therefore, monitoring and
114 quantifying human interference in Xiong'an New Area can ensure its strategic target of
115 future planning.

116 In this study, we take the human-dominated Xiong'an New Area, which is a typical
117 heterogeneous region in China, as the study area and aim to demonstrate a detailed
118 spatial pattern and the dynamics of the HANPP from 2000 to 2018. Accordingly, we
119 use the spatial and temporal nonlocal filter-based fusion model (STNLFFM), which has
120 been proven to generate a robust prediction for the time series research in a
121 heterogeneous region (Cheng et al. 2017), to generate time series fusion images with
122 30 m spatial resolution by blending Landsat Thematic Mapper (TM), Enhanced
123 Thematic Mapper Plus (ETM+), Operational Land Imager (OLI) series with Terra
124 Moderate Resolution Imaging Spectroradiometer (MODIS) MOD09A1 series. The
125 common HANPP framework is utilized to estimate HANPP with a fine spatial
126 resolution based on the fused images (Haberl et al. 2007). The spatial pattern and trend
127 for both the HANPP and its subcomponents are analyzed using the Mann–Kendall (M–

128 K) trend analysis approach. In addition, the relationship between the HANPP and the
129 natural-, social-, and economic-driven factors is discussed, respectively. The results of
130 this study contribute to the deep understanding of the background characteristics of
131 vegetation in Xiong'an New Area, which will further help in the green development,
132 urban planning, and decision making of the new area.

133 **Materials and methods**

134 **Study area**

135 Xiong'an New Area is located in the center of Hebei Province (Fig. 1, 38°43'–39°0'
136 N, 115°38'–116°20' E). The agricultural land in Xiong'an New Area accounted for more
137 than half of the total area in 2016 (Tang et al. 2020b). The new area construction will
138 expand the region from 1566 km² to 2000 km² in the future (Xu et al. 2018). Winter
139 wheat and summer corn are the major crops in this area (Wang et al. 2017a; Wang et
140 al. 2017b), and there are both ripe once a year and ripe twice a year for agriculture (Tang
141 et al. 2020b). Xiong'an New Area has a warm temperate monsoon continental climate
142 with the annual temperature and precipitation of 12.1 °C and 560 mm, respectively (Xu
143 et al. 2018). Human interferences generally concentrate on agriculture production and
144 urban construction.

145

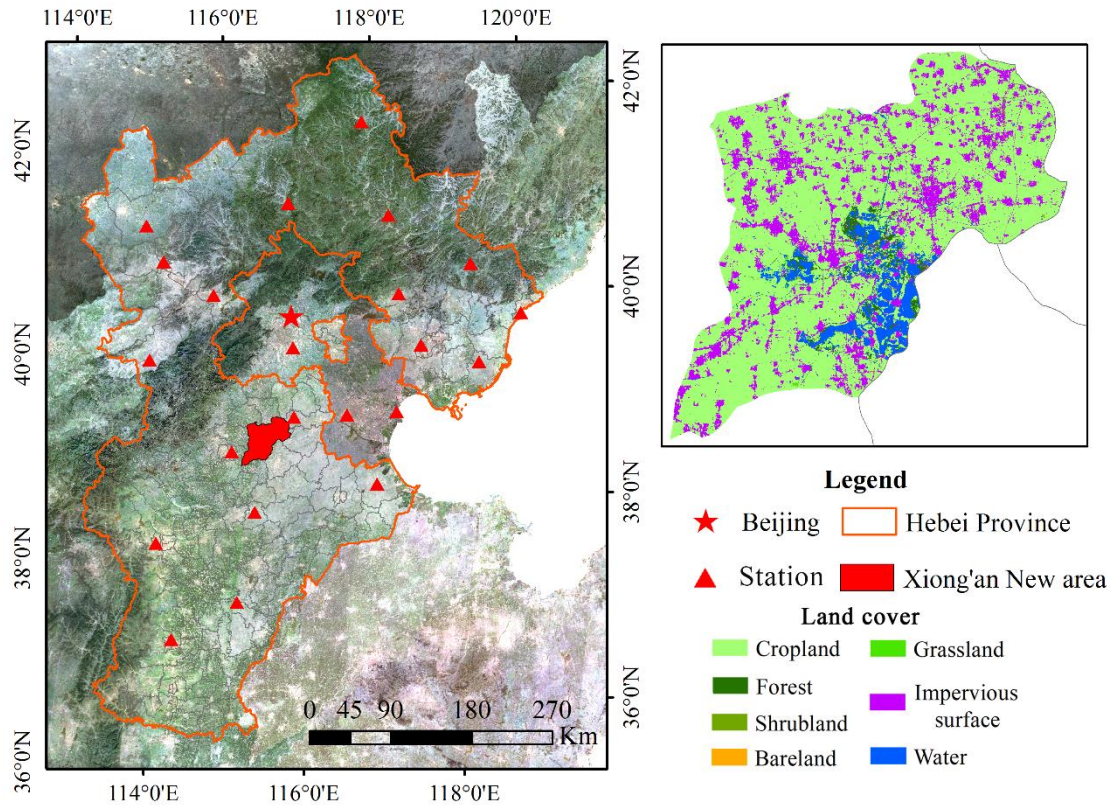


Fig. 1. Location and land cover map of Xiong'an New Area

Datasets and processing

The remote sensing, land use, meteorological station, and economic statistic data were all integrated into the HANPP framework (Table 1). The remote sensing data covered the atmospherically corrected surface reflectance products of Landsat TM/ETM+/OLI and the MOD09A1 products of Terra MODIS (Collection 6). All products were collected and preprocessed in the Google Earth Engine platform. The preprocessing mainly included two steps: 1) calibration between TM/ETM+ and OLI to document the sensor differences and generate the temporal continuous reflectance data in the study period according to the previous study (Roy et al. 2016); and 2) georeferencing between Landsat and MODIS to meet the input requirement of the STNLFFM method (Cheng et al. 2017). The meteorological data included daily

160 temperature, daily precipitation, and daily sunshine duration from 22 national
161 meteorological stations in the BTH region. All data were converted into month data by
162 summing up or averaging the daily data in each month at each station. The monthly
163 total solar radiation was calculated based on the daily sunshine duration data ([Wang et](#)
164 [al. 2017a](#)). All station data were interpolated into rasters, consistent with the remote
165 sensing data, through the Inverse Distance Weighted method. The economic statistic
166 data covered 12 kinds of main crops and wood harvested data, agricultural condition
167 data, and social–economic data. The harvested data were available only for political
168 units and did not match the remote sensing data. Hence, we assumed the same crop
169 (wood) yield per unit of cropland (forest) in Xiong'an New Area and distributed the
170 yield to each pixel based on the land cover map ([Li and Meng 2018](#)). We also collected
171 three phases of land cover product data with 30 m spatial resolution in Xiong'an New
172 Area.

173

174

175

176

177

178

179

180

181

182

183

184

Table 1. Data sources for HANPP framework input.

Data	Feature	Range	Source	Use
Remote sensing data	TM, ETM+, OLI, MOD09A1	2000-2018	Google Earth Engine platform	NPP
Meteorological station data	temperature, precipitation, sunshine duration	2000-2018	China Meteorological Administration (http://data.cma.cn/en)	NPP
Economic statistic data	Food crop (rice, wheat, maize, etc.), Economic crop (Peanuts, sesame, cotton vegetables, fruits, etc.), wood, GDP, fertilizer, non-agricultural population, available irrigated area	2000-2018	Economic Statistics Yearbook of Baoding city	HANPP _{harv}
Land cover data	Land use	2010, 2015, 2017	Tsinghua University (http://data.ess.tsinghua.edu.cn/)	NPP

186

187 **Methods**

188 STNLFFM algorithm

189 The STNLFFM algorithm searched the similar pixels of each pixel in fine-
 190 resolution reflectance images with the help of the pixel differences in both fine- and
 191 coarse-resolution images and fully used the high degree of spatio-temporal redundancy
 192 in the remote sensing image sequence to produce the final prediction (Cheng et al. 2017).
 193 The procedures of the algorithm are divided into three steps: 1) similar pixel selection;
 194 2) similar pixel weight calculation; and 3) regression coefficient calculation.

195 In the first step, two constrains were used to select the similar pixels of each target
 196 pixel: 1) similar pixels must have the same type of land cover; and 2) similar pixels

197 must have a similar change with the target pixel in a certain period. The two constrains
 198 are calculated as follows:

$$199 \quad \left| F(x_i, y_j, B, t_k) - F(x, y, B, t_k) \right| \leq d \times 2^{F(x, y, B, t_k)} \quad (1)$$

$$200 \quad \left\| C(x_i, y_j, B, t_k) - C(x_i, y_j, B, t_p) \right\| - \left\| C(x, y, B, t_k) - C(x, y, B, t_p) \right\| < \sigma_{cc} \quad (2)$$

201 where, $F(x_i, y_j, B, t_k)$ and $C(x_i, y_j, B, t_k)$ represent the value of the Landsat and
 202 MOD09A1 images at position (x_i, y_j) , Band B , and date t_k ; d indicates the
 203 threshold coefficient (i.e., 0.01); and σ_{cc} represents the uncertainty of the MOD09A1
 204 temporal differences caused by the atmosphere changing from t_k to t_p (i.e., 0.005
 205 based on Cheng's experiments).

206 In the second step, the weight of similar pixels included two parts: 1) individual
 207 weight of each similar pixel and 2) whole weight of each fine-resolution image.
 208 Considering the unknown of the Landsat image at the prediction date t_p , the nonlocal
 209 filter was used to obtain the individual weight based on the MOD09A1 images.
 210 Meanwhile, the whole weight was calculated based on the temporal difference of the
 211 MOD09A1 images from t_k to t_p according to the principle that a closer temporal
 212 distance had a larger weight. The individual and whole weights were integrated to
 213 obtain the final weight. All equations are calculated as follows:

$$214 \quad W_{individual}(x_i, y_i, B, t_k) = \exp \left(- \frac{G * \left\| C(P(x_i, y_i, B, t_k)) - C(P(x, y, B, t_p)) \right\|}{h^2} \right) \quad (3)$$

$$215 \quad W_{whole} = \frac{1 / \sum_{(i,j) \in \Omega} \left(\left\| C(P(x_i, y_j, B, t_k)) - C(P(x_i, y_j, B, t_p)) \right\| \right)}{\sum_k \left(1 / \sum_{(i,j) \in \Omega} \left(\left\| C(P(x_i, y_j, B, t_k)) - C(P(x_i, y_j, B, t_p)) \right\| \right) \right)} \quad (4)$$

$$216 \quad W(x_i, y_j, B, t_k) = W_{ind}(x_i, y_j, B, t_k) \times W_{whole} \quad (5)$$

217 where, h represents the noise in the MOD09A1 images (i.e., 0.15); G is a Gaussian
 218 kernel; $C(P(x_i, y_j, B, t_k))$ is the coarse-resolution image value of patch P centered at
 219 pixel (x_i, y_j) ; P is determined by the zoom relationship of the spatial resolution
 220 between the Landsat and MOD09A1 images; and Ω indicates a local window.

221 In the final step, the gain coefficient and the bias of were calculated using the
 222 restricted least-squares model based on the available coarse-resolution reflectance
 223 images. The final prediction could be obtained as the following equation, and more
 224 detail information can be found in [Cheng et al. \(2017\)](#).

$$225 \quad F(x, y, B, t_p) = \sum_{k=1}^M \sum_{i=1}^N W(x_i, y_i, B, t_k) \times [a(x_i, y_i, B, \Delta t_k) \times F(x_i, y_i, B, t_k) + b(x_i, y_i, B, \Delta t_k)] \quad (6)$$

226 where, $F(x, y, B, t_p)$ indicates the final predicted image. M, N represent the
 227 number of input Landsat–MOD09A1 images and similar pixels, respectively; and a, b
 228 represent the gains and bias coefficient of the fine-resolution images from t_k to t_p ,
 229 respectively.

230 HANPP framework

231 In this study, the HANPP followed the widely defined framework used in the
 232 previous study, which calculated the HANPP as follows ([Haberl et al. 2007](#); [Andersen
 233 et al. 2015](#)).

$$234 \quad HANPP = NPP_{pot} - NPP_{act} + HANPP_{harv} \quad (7)$$

235 where, NPP_{pot} , NPP_{act} , $HANPP_{harv}$ represent the potential, actual and harvested NPPs,
 236 respectively. NPP_{pot} indicates the amount of NPP provided by the ecosystem without
 237 human disturbance, while NPP_{act} , $HANPP_{harv}$ indicate the actual NPP in a real
 238 ecosystem condition and the harvested NPP via human activities, respectively.

239 The potential and actual NPPs were calculated using our improved CASA model,
240 which was further calibrated by field observed data in China (Zhu et al. 2007), and
241 considered the land cover change (Wang et al. 2018). The improved CASA model
242 thought that the NPP comprised absorbed photosynthetically active radiation (APAR)
243 and light utilization efficiency (ε).

$$244 \quad NPP = APAR_{(x,t)} * \varepsilon_{(x,t)} \quad (8)$$

245 where, x, t denote the spatial position and the time, respectively, and $APAR_{(x,t)}$ is
246 derived as follows.

$$247 \quad APAR_{(x,t)} = SOL_{(x,t)} * FPAR_{(x,t)} * 0.5 \quad (9)$$

248 where, $SOL_{(x,t)}$ represents total solar radiation at position x and time t , and $FPAR_{(x,t)}$
249 indicates the absorption ratio of the solar radiation. The constant (0.5) represents that
250 only half of the total solar radiation from the Sun can be useful for vegetation
251 (wavelength: 0.4 μm to 0.7 μm). $FPAR_{(x,t)}$ and $\varepsilon_{(x,t)}$ can be further calculated based
252 on the previous study (Wang et al. 2018). Meanwhile, considering the human
253 interference on cropland and built-up land, we adjusted the CASA model parameters
254 for these two land cover types to calculate the potential NPP according to Hua's
255 research (Hua 2009).

256 The harvested NPP was made of the NPP derived from the cropland, built-up land,
257 and forest. The cropland-harvested NPP included the edible and crop residue part. Both
258 parts were converted into the carbon content value using the method in Zhang's study,
259 which was based on the crop's statistical yield, straw coefficient, dry matter fraction,
260 carbon fraction, and recover rate (Zhang et al. 2015). These crop-specific parameters

261 could be obtained from former studies (Table 2) (Haberl et al. 2007; Huang et al. 2007;
262 Xie et al. 2011; Wang et al. 2012).

263

264 Table 2 Straw coefficient, dry weight fraction, carbon fraction and recovery rate of main crops

Crop	Straw coefficient	Dry matter fraction	Carbon fraction of edible part	Carbon fraction of edible part	Recover rate
Rice	0.95	0.85	0.38	0.42	0.2
Wheat	1.22	0.85	0.39	0.49	0.2
Maize	1.05	0.78	0.39	0.47	0.2
Sorghum	1.6	0.91	0.45	0.45	0.2
Soybean	1.36	0.85	0.40	0.45	0.5
Potato	0.42	0.20	0.39	0.42	0.25
Batata	0.53	0.20	0.39	0.42	0.25
Peanut	0.86	0.885	0.38	0.38	0.2
Rape	2.57	0.90	0.42	0.45	0.3
Sesame	1.78	0.85	0.40	0.45	0.2
Cotton	2.62	0.90	0.40	0.39	0.2
Vegetable	0.1	0.1	0.475	0.475	0.2
Fruit	0.15	0.15	0.475	0.475	0.2

265

266 We assumed that the forest-harvested NPP was sourced from the timber yield. The
267 corresponding carbon contents were calculated based on the wood density and carbon
268 fraction derived from Haberl's study (Haberl et al. 2007). Meanwhile, the NPP values
269 were calculated as the timber yield multiplied by wood density and carbon fraction.
270 Considering the data availability, we took half of the actual NPP as the built-up land-
271 harvested NPP according to the former study (Fetzel et al. 2014).

272 Trend analysis method

273 In this study, M–K was utilized to demonstrate the spatial trend of both the HANPP
274 and its subcomponents (Mann 1945). M–K is one of widely used nonparametric test

275 methods in the field of meteorology, ecology, and agriculture (Burn and Elnur 2002;
 276 Xu et al. 2004). The M-K test statistic was calculated as follows:

$$277 \quad S = \sum_{k=1}^{n-1} \sum_{j=k+1}^n \text{sgn}(x_j - x_k) \quad (10)$$

278 where x_i, n represent the data sequence value and length, respectively, and sgn is
 279 calculated as follows:

$$280 \quad \text{sgn}(x_j - x_i) = \begin{cases} 1 & \text{if } x_j > x_i \\ 0 & \text{if } x_j = x_i \\ -1 & \text{if } x_j < x_i \end{cases} \quad (11)$$

281 Based on the M-K test theory, S followed a normal distribution when n was
 282 larger than 8. The S expectation and variance are expressed as the follows:

$$283 \quad E(S) = 0 \quad (12)$$

$$284 \quad V(S) = \frac{n(n-1)(2n+5) - \sum_{m=1}^n t_m m(m-1)(2m+5)}{18} \quad (13)$$

285 where, t_m is the value of extent m . Therefore, the normalized test statistics Z could
 286 be derived as the follows:

$$287 \quad Z = \begin{cases} \frac{S-1}{\sqrt{V(S)}} & S > 0 \\ 0 & S = 0 \\ \frac{S+1}{\sqrt{V(S)}} & S < 0 \end{cases} \quad (14)$$

288 When $|Z|$ was larger than 1.65, 1.98, and 2.58, the trend had significant levels (p)
 289 corresponding to 0.1, 0.05, and 0.01, respectively. To further understand the trend
 290 magnitude, we applied the robust trend estimator developed by Sen (1968) to calculate
 291 the trend slope as follows (Sen and Kumar 1968).

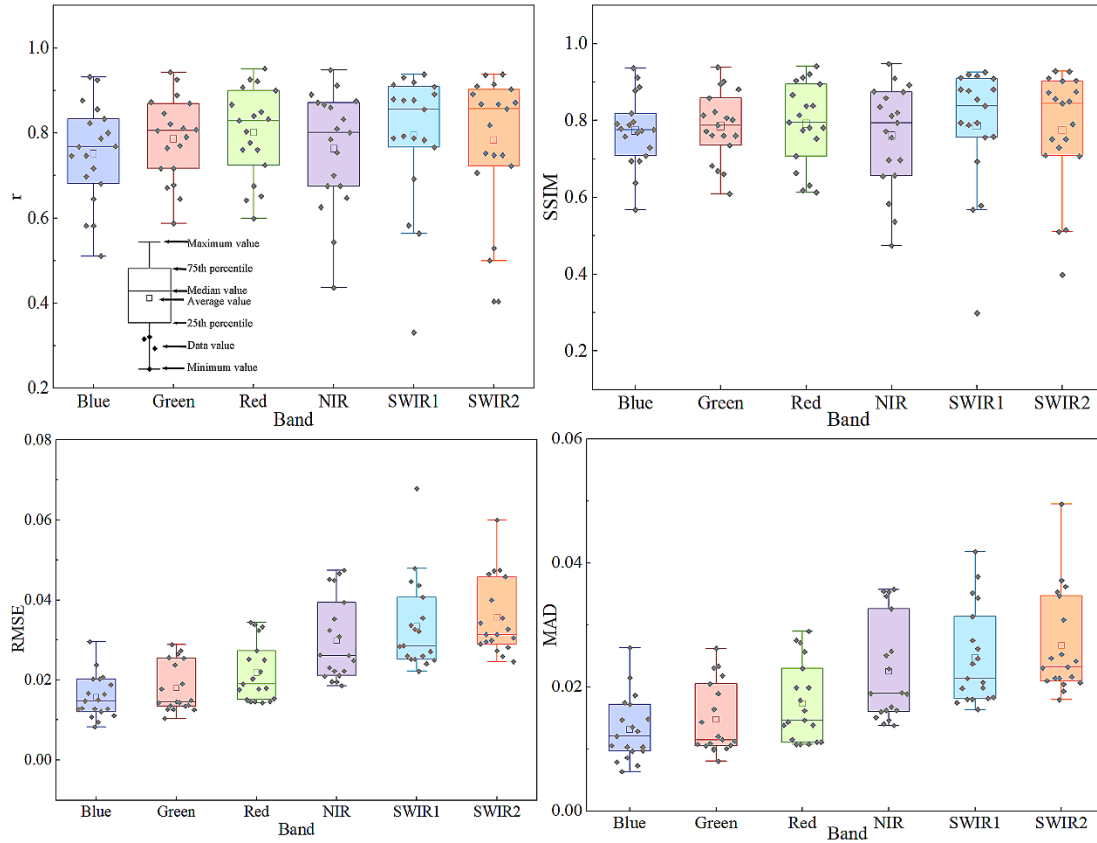
$$292 \quad \text{slope} = \text{Median} \left(\frac{x_j - x_i}{j - i} \right) (1 \leq i < j \leq n) \quad (15)$$

293 where, slope indicates the monotonic increase (positive) or decrease rate (negative) of
294 the data sequence.

295 **Results**

296 **Generation of time series fusion images**

297 We obtained six-band (i.e., blue, green, red, NIR, SWIR1, and SWIR2) time series
298 monthly fusion images from 2000 to 2018 based on the STNLFFM approach. Multiple
299 testing indicators, including correlation coefficient (r), root mean square error (RMSE),
300 structural similarity index (SSIM), and mean absolute deviation (MAD), were used to
301 validate the accuracy of the fusion images. The box plot in Fig. 2 shows that all the
302 indicators were distributed in the 1.5 times inter-quartile range ($1.5 * IQR$), except for
303 only few data points, in SWIR1 and SWIR2 band, exhibited abnormalities. Furthermore,
304 most data points especially concentrated inside the box (25th to 75th percentile). The
305 average values of r and SSIM were above 0.75 and 0.76, respectively, while those of
306 the RMSE and MAD were lower than 0.035 and 0.026, respectively. Among the six
307 spectral bands, the testing results of the red and NIR bands, which were sensitive to the
308 vegetation, had better accuracies with r and SSIM of up to 0.8 and 0.79, respectively,
309 and RMSE and MAD of up to 0.022 and 0.017, respectively.



310

311 Fig. 2 Accuracy of multiple indicators for the fusion images from 2000 to 2018: (a) r, (b) SSIM,
 312 (c) RMSE, and (d) MAD

313

314 We calculated the NDVI differences (Δ NDVI) between the NDVI based on the
 315 fusion images and that based on the observed images to further verify the accuracy of
 316 the NDVI derived from the fusion images. Compared with the monthly NDVI images
 317 from 2000 to 2018 (Fig. 3), Δ NDVI for all months were mainly concentrated in the
 318 range of 0–0.15. Moreover, the differences in February, August, and September were
 319 better than those of the other months with $1.5 * IQR$ less than 0.1. The average
 320 differences of February, August, and September were 0.05, 0.04, and 0.03, respectively.

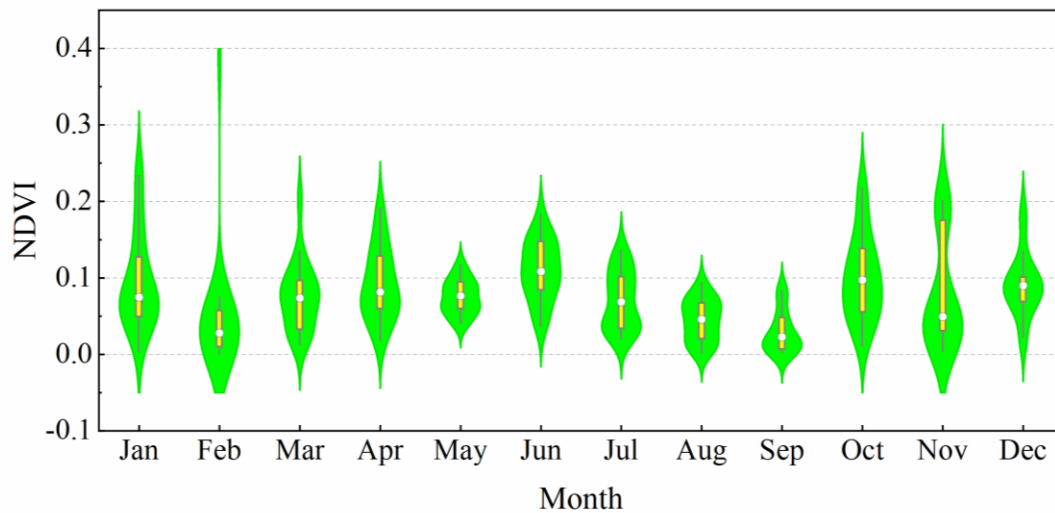


Fig. 3 Δ NDVI distribution of each month from 2000 to 2018

321

322

323

324 Change of subcomponents and HANPP

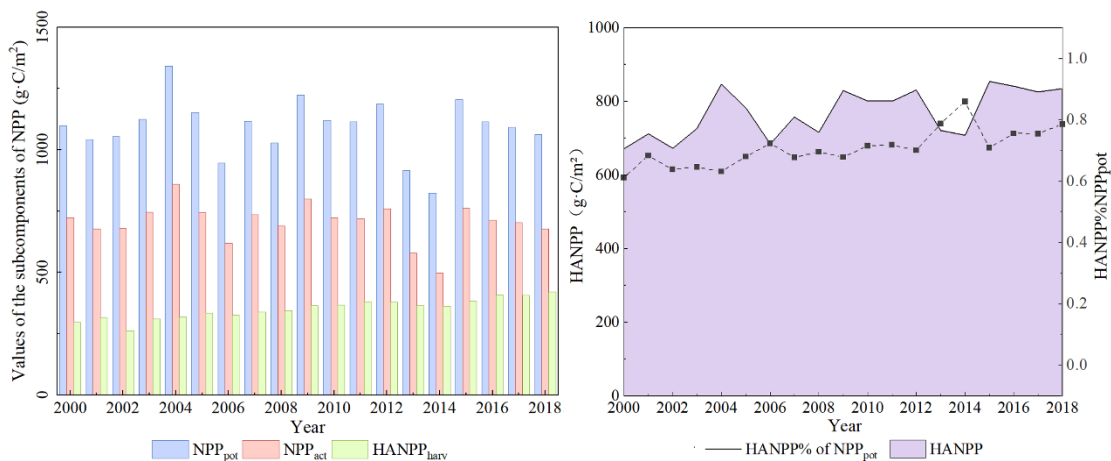
325 According to the abovementioned methods, we could obtain the dynamics of both

326 the HANPP and its subcomponents based on the fusion images (Fig.4). Fig. 4(a) depicts

327 that NPP_{pot} and NPP_{act} exhibited fluctuating changes, while $HANPP_{harv}$ showed a slight

328 increase in change from 2000 to 2018. Meanwhile, Fig. 4(b) demonstrates that the

329 HANPP was larger than $670 \text{ g} \cdot \text{C}/\text{m}^2$, and $HANPP\% NPP_{pot}$ was above 60%.



330

331 Fig. 4 Change of the HANPP and its subcomponents and the ratio to NPP_{pot} : (a) subcomponents

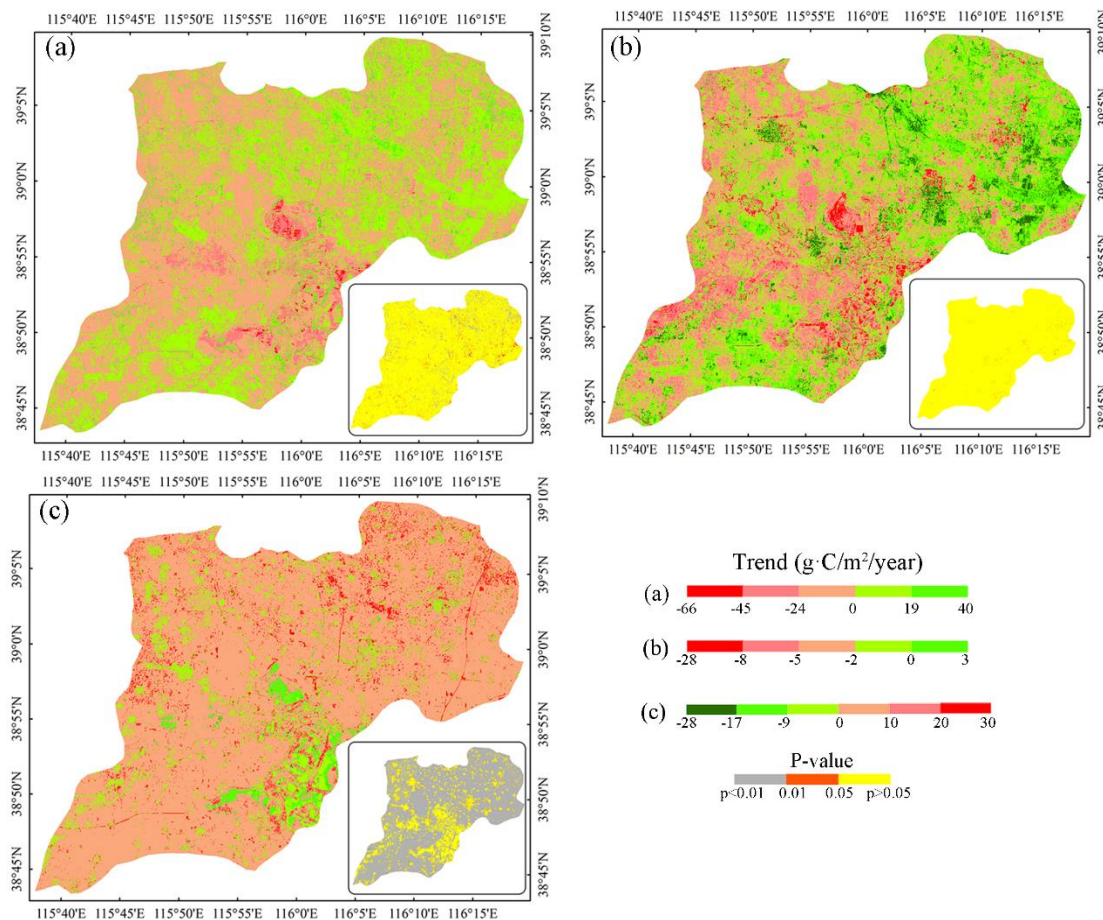
332

and (b) HANPP

333

334 Fig. 5 displays the spatial trends and the corresponding significant level (P-value),
 335 of the three HANPP subcomponents. NPP_{pot} and NPP_{act} had similar change laws of the
 336 increasing trend occurring in the southern and northeastern Xiong'an New Area and the
 337 decreasing trend concentrating in the middle area (Figs. 5(a) and (b)). However, both
 338 uptrend and downtrend showed non-significant levels. $HANPP_{harv}$ displayed an
 339 increasing trend in the total area, except for the southeastern area covered in water and
 340 unsuitable for agriculture or urban construction (Fig. 5(c)). The uptrends had a very
 341 significant level ($P < 0.01$).

342



343

344 Fig. 5 Spatial trend and corresponding significant level of the HANPP subcomponents: (a) NPP_{pot} ;

345

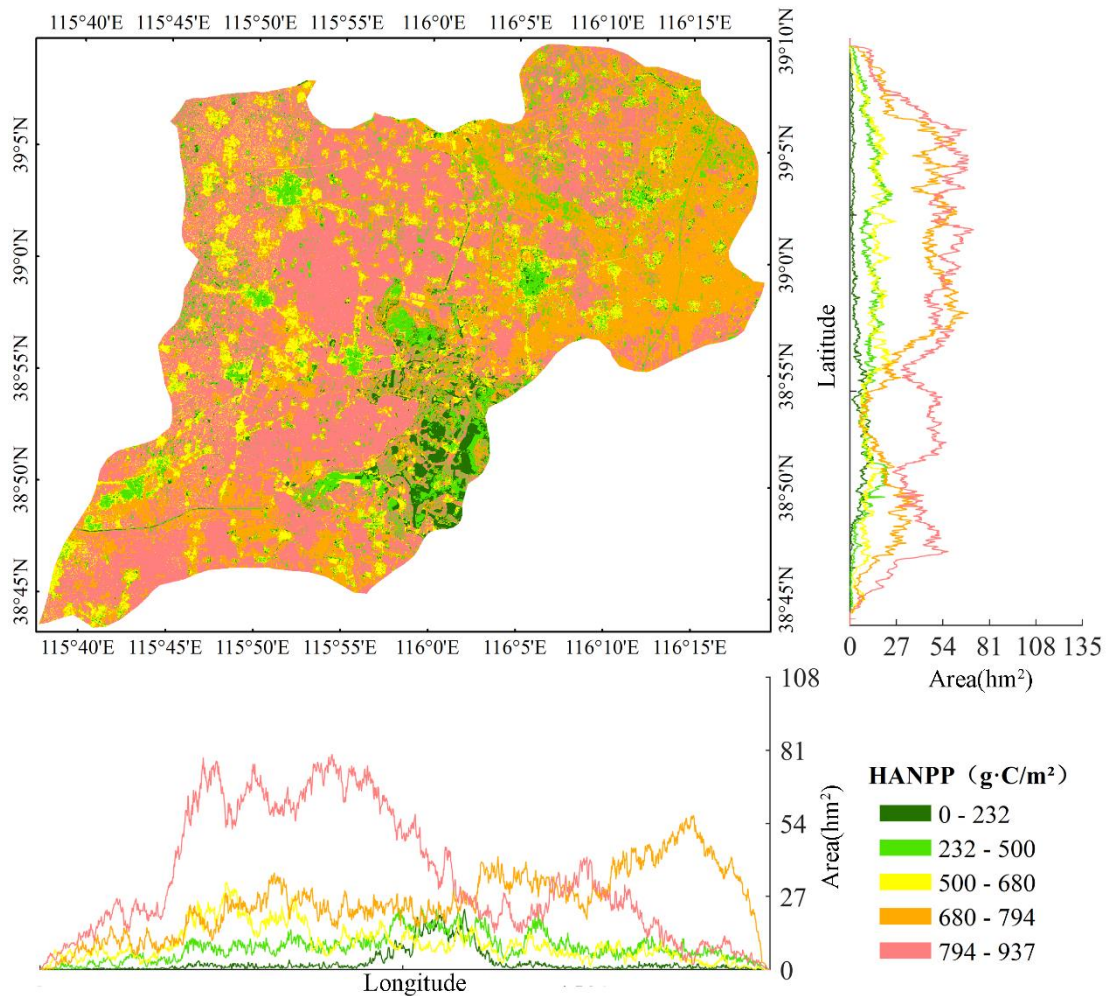
(b) NPP_{act} ; and (c): $HANPP_{harv}$

346

347 **Spatial pattern and trend of the HANPP**

348 We obtained the HANPP spatial pattern (Fig. 6) based on the results of NPP_{pot} ,
349 NPP_{act} , and $HANPP_{harv}$ and found that the HANPP varied across the whole area. The
350 highest HANPP level emerged in the region with a longitude between the $115^{\circ}40'E$ and
351 $116^{\circ}E$, while the higher HANPP levels prevailed with a latitude increase. Some built-
352 up and the water areas held a relatively low HANPP of less than $500\text{ g}\cdot\text{C}/\text{m}^2$ as a
353 consequence of low agricultural intensity.

354



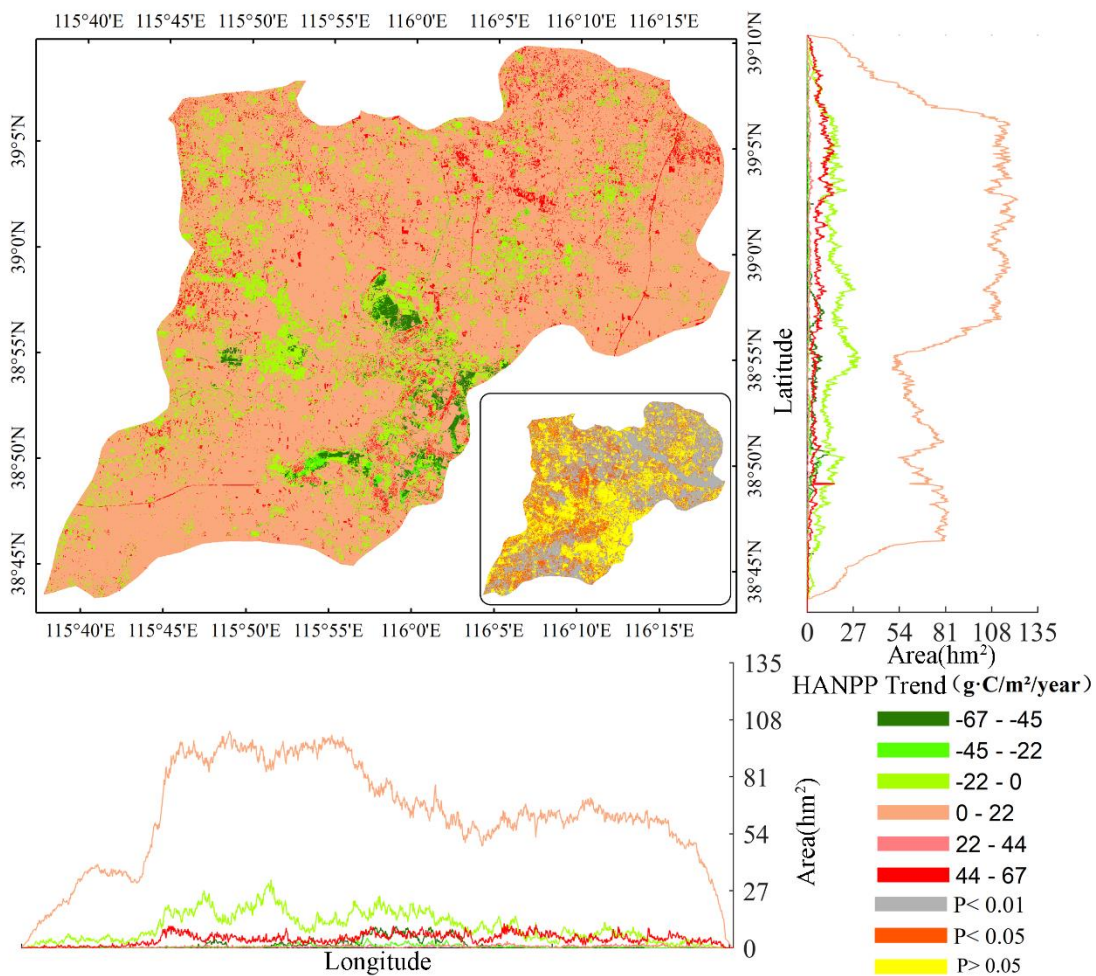
355

356

Fig. 6 Spatial pattern of the HANPP in Xiong'an New Area

357

358 Fig. 7 demonstrates the spatial trend of HANPP, from which we found most of the
 359 regions showed an increasing trend with a magnitude of less than 22 g·C/(m²·year),
 360 while the southeastern area and some discreted western area had a decreasing trend.
 361 Both along with the latitude and longitude, the trends held an increasing change (0-22
 362 g·C/(m²·year)) from 2000 to 2018. The trend expressed an extremely significant level
 363 (P < 0.01) in the northeastern and southern areas and a significant level (P < 0.05) in
 364 the middle and northwestern regions. In contrast, a non-significant level was observed
 365 in the southeastern area.
 366



367
 368 Fig. 7 Spatial trend of the HANPP in Xiong'an New Area
 369

370 Discussion

371 Correlation between climate factors and the HANPP

372 Temperature and precipitation are two climate factors related to the geographical
373 distribution of vegetation, which are important to the NPP in a dryland ecosystem
374 (Wang et al. 2019). Among all climate factors, precipitation has the greatest influence
375 on the vegetation cover changes (Zhou et al. 2019), is further related to the crop yield
376 in the Hebei region (Wang et al. 2020). In this study, we mapped the spatial correlation
377 between temperature, precipitation and HANPP at pixel level based on the
378 meteorological raster data. According to Fig. 8(a), the HANPP showed a low correlation
379 with temperature across most parts of Xiong'an New Area, with the correlation
380 coefficient ranging from -0.39 to 0.39 and the significant level $P > 0.1$. These results
381 reflected the same phenomenon of the NPP being not significantly correlated with the
382 average annual temperatures in Hebei (Wang et al. 2018). From Fig. 8(b), we concluded
383 that HANPP in most cropland region held the significant correlation with precipitation,
384 whose coefficients were larger than 0.46 ($P < 0.05$). The results was consistent with the
385 previous study that precipitation played main role in crop yields or harvested HANPP
386 (Wang et al. 2017a). Since the precipitation was closely linked to latitude in Hebei
387 (Zhao et al. 2018), even larger correlation coefficient (>0.58) with an extremely
388 significant level ($P < 0.01$) were observed on the northern cropland. Notably, the
389 correlation was regarded as extremely and significantly negative because some regions
390 in southeastern Xiong'an New Area were always covered by water from 2000 to 2018,
391 causing them to lack human appropriation.

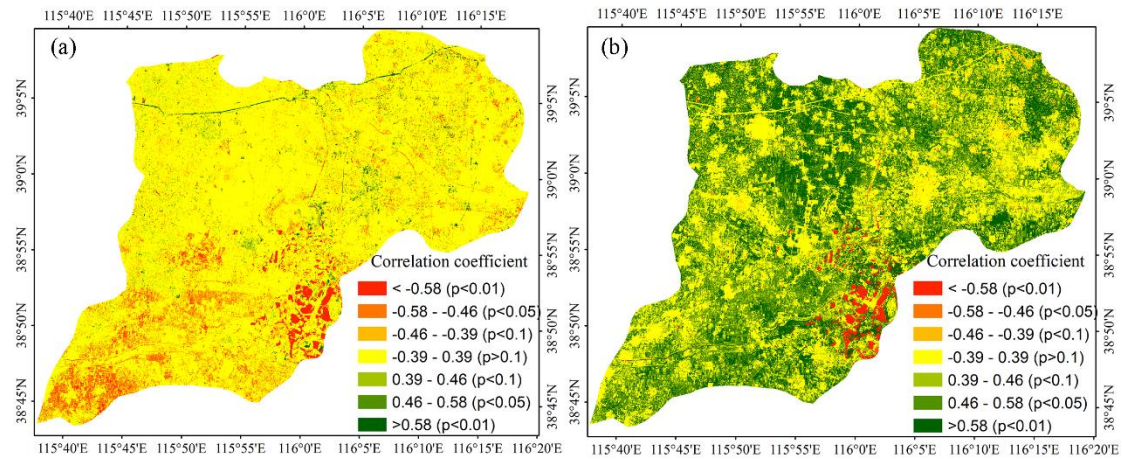
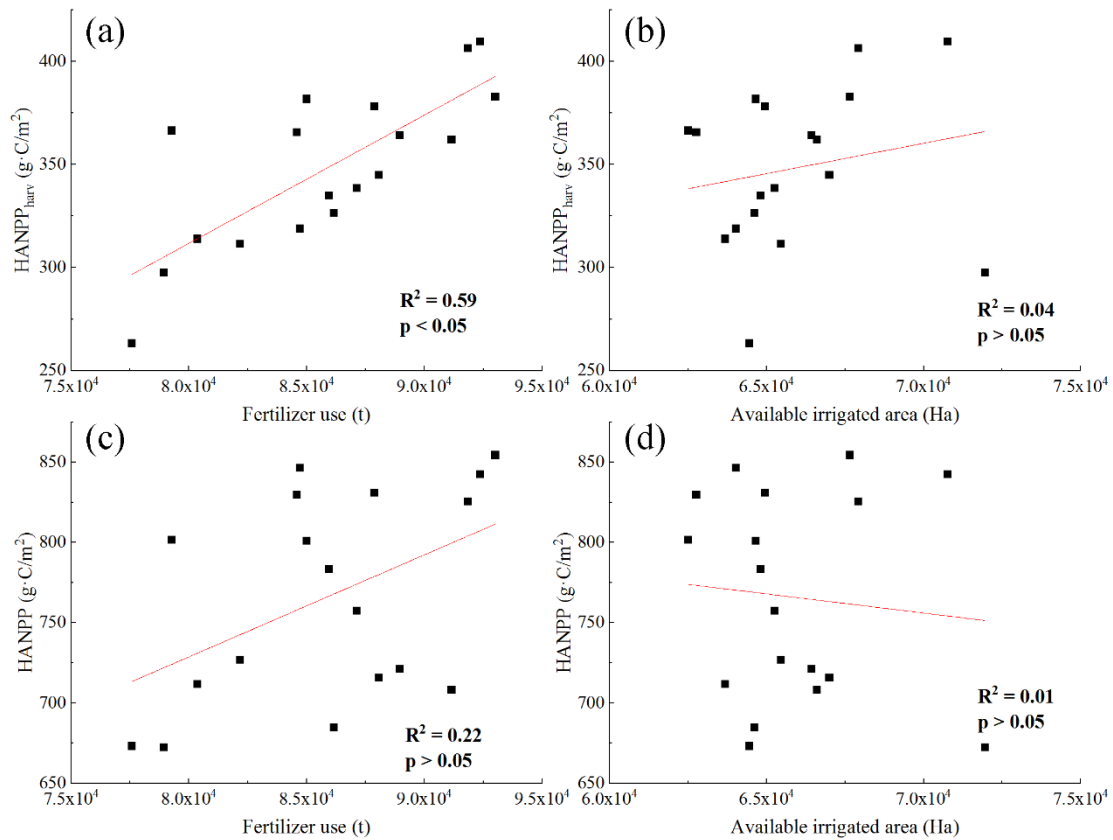


Fig. 8 Correlation between climate factors and the HANPP in Xiong'an New Area: (a) temperature and (b) precipitation

Influences of agricultural conditions on the HANPP

Agriculture dominates in Xiong'an New Area; hence, agricultural conditions may play an important role in the HANPP dynamics. A previous study identified fertilizer use and irrigation area as two main agricultural-driven factors for the determination of the HANPP amount (Krausmann et al. 2012). Therefore, we also analyzed herein the driving relationship between these agricultural conditions (i.e., amount of fertilizer and available irrigated area) with the HANPP elements (i.e., HANPP_{harv} and HANPP). Figs. 9(a)–(c) depict that HANPP_{harv} and HANPP responded to the amount of fertilizer with determination coefficients (R^2) equal to 0.59 and 0.22, respectively. These results indicate that fertilizer use could prompt the agricultural production to some extent. The conclusions were similar to those obtained for the same agricultural ecosystem in the coastal areas of Jiangsu (Zhang et al. 2015). However, note that the change of the available irrigated area had a low influence on the HANPP elements ($R^2 < 0.04$) because even a limited irrigation could achieve a relatively high agricultural production

410 through the enhanced water use efficiency (Xu et al. 2016). The irrigation capacity was
 411 no longer the main limiting factor on production in Xiong'an New Area as a
 412 consequence of the developed agriculture technology.
 413

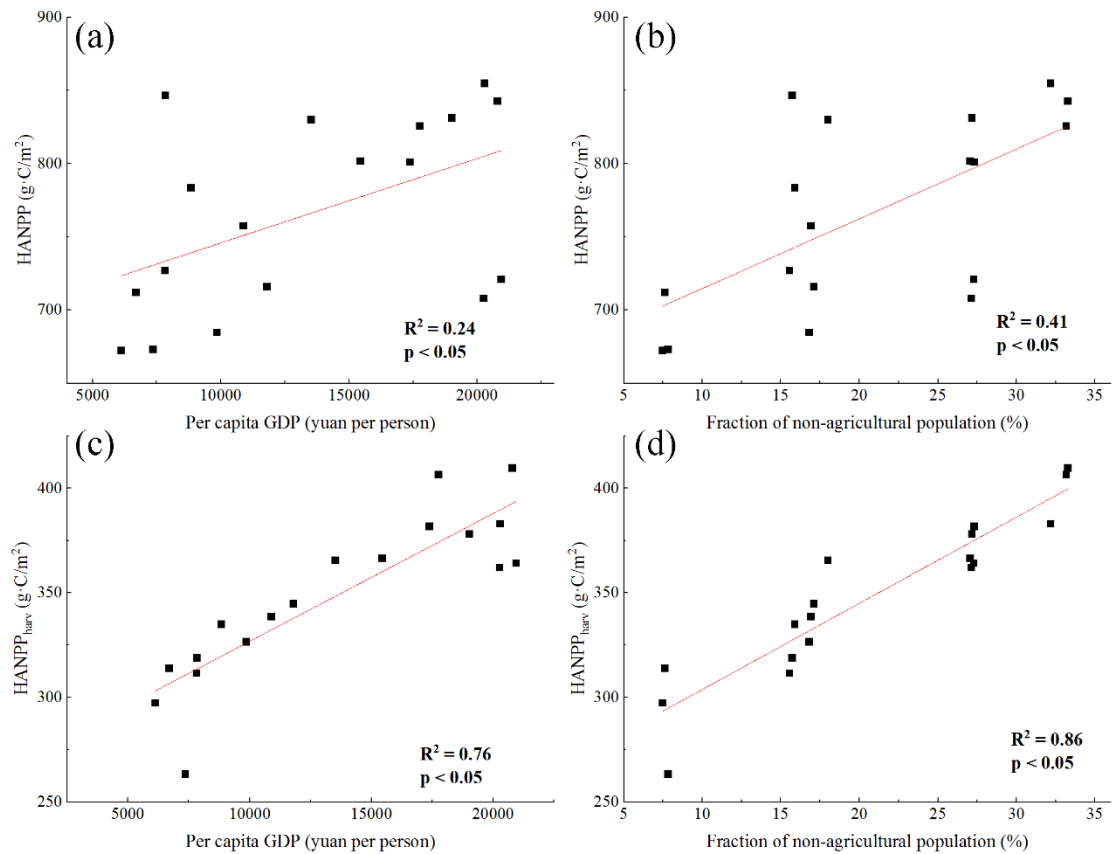


414
 415 Fig. 9 Correlation of agricultural conditions with the HANPP elements: (a) fertilizer use and
 416 HANPP_{harv}; (b) available irrigated area and HANPP_{harv}; (c) fertilizer use and HANPP; and (d)
 417 available irrigated area and HANPP

418 **Influences of socio-economic conditions on the HANPP**

419 HANPP integrates socio-economic conditions with natural dimensions, which
 420 demonstrate a positive correlation with a region's population (Krausmann et al. 2012;
 421 Erb et al. 2013). Accompanied by urbanization and economic development, especially
 422 after the proposal of the Xiong'an New Area construction, how socio-economic

423 conditions are related to the HANPP should be mastered. The per capita GDP (yuan per
424 person) and the fraction of the non-agricultural population were selected herein as the
425 socio-economic indicators for analyzing the HANPP element response to these factors
426 in Xiong'an New Area. (Niedertscheider et al. 2017). We conclude that both the per
427 capita GDP and the fraction of the non-agricultural population had a relatively low
428 impact on the HANPP, with R^2 equal to 0.24 and 0.41, respectively (Fig. 10). The small
429 R^2 also demonstrated that the construction and the development of Xiong'an New Area
430 would not bring extensive growth of human appropriation on the ecosystem and violate
431 its SDG. However, human occupation on the built-up area would increase because of
432 the forthcoming urban expansion and population growth (Xu et al. 2018). Therefore,
433 R^2 between per capita GDP and $\text{HANPP}_{\text{harv}}$ (0.76), fraction of the non-agricultural
434 population and $\text{HANPP}_{\text{harv}}$ (0.86) reflected the great relationship of social development
435 to human-harvested NPPs.



436

437

438

439

440

441 Comparison with previous studies on the HANPP

442

443

444

445

446

447

448

449

Fig. 10 Correlation between the socio-economic conditions and the HANPP elements: (a) per capita GDP and HANPP; (b) fraction of the non-agricultural population and the HANPP; (c) per capita GDP and HANPP_{harv}; and (d) fraction of the non-agricultural population and HANPP_{harv}

The HANPP%NPP_{pot} proportion is a comparable indicator for assessing the level of appropriated NPP by human activities among different countries and regions (Huang et al. 2020). Table 3 shows that reports in different study areas had distinct HANPP%NPP_{pot} results, which, on the one hand, may be caused by the different definitions of and calculation methods for the HANPP (Haberl et al. 2007), and on the other hand, may be caused by the heterogeneity of the study area to a large extent (Andersen et al. 2015). Our study, which considered human extraction from cropland, built-up land, and forest, obtained HANPP%NPP_{pot} values ranging from 62% to 82%.

450 These results were higher than those obtained from research in the coastal areas of
 451 Jiangsu, the similar agricultural dominated region that only considered the cropland-
 452 harvested NPP (Zhang et al. 2015). However, our results were consistent with those
 453 acquired for some developed Europe countries, including United Kingdom, Hungary,
 454 and Italy, which have a large proportion of cropland and a high level of agricultural
 455 modernization (Kohlheb and Krausmann 2009; Musel 2009; Niedertscheider and Erb
 456 2014).

457

458 Table 3 Comparisons between the estimates of the HANPP rate in this study and those in the
 459 previous studies

Reference	Scale	Year	HANPP%NPP _{pot}
this study	Xiong'an New Area (China)	2000-2018	62-82
(M. et al. 1986)	Global	1970s	30.7
(Haberl et al. 2007)	Global	2000	23.8
(Haberl et al. 2001)	Austria	1950-1995	51
(Kastner 2009)	Philippines	1910-2003	35-62
(Kohlheb and Krausmann 2009)	Hungary	1961-2005	67-49
(Musel 2009)	United Kingdom	1800-2000	71-68
(Schwarzlmuller 2009)	Spain	1955-2003	67-61
(Niedertscheider and Erb 2014)	Italy	1884-2007	78-56
(Niedertscheider et al. 2012)	South Africa	1961-2006	21-25
(Chen et al. 2015)	China	2001-2010	49.5-57.8
(O'Neill et al. 2007)	Nova Scotia (Canada)	1999-2003	25.5
(Zhang et al. 2015)	Coastal areas of Jiangsu (China)	2000-2010	50.3-71
(Li and Meng 2018)	Heihe River basin (China)	2001-2013	38-71
(Huang et al. 2020)	Yangtze River Delta	2005-2015	59-72

460

461 **Impacts, limitations and future work**

462 HANPP accounted both the loss and harvested part of NPP caused by human
 463 development, which served as a feasible evaluating tool for regional SDG (Bishop et

464 [al. 2010; Ha et al. 2012](#)). Our improved HANPP estimation and dynamics simulation
465 for a long time series could further sustain the scientific construction of the new area.
466 For example, the 30 m spatial resolution HANPP could help us master the spatial
467 pattern of $\text{HANPP}/\text{NPP}_{\text{pot}}$ in a fine grid level, from which we could determine how
468 the high or low values are distributed (a distribution map). Since the higher
469 $\text{HANPP}/\text{NPP}_{\text{pot}}$ meant the less fraction of NPP supported by other species ([Haberl et](#)
470 [al. 2004](#)), the new area construction should fully consider the distribution map.
471 Meanwhile, NPP loss (NPP_{luc}) caused by human induced land cover change (NPP_{pot}
472 minus NPP_{pot}) could also be calculated in fine grid level and compared with $\text{HANPP}_{\text{harv}}$.
473 Furtherly, the higher ($\text{NPP}_{\text{luc}} < \text{HANPP}_{\text{harv}}$) or lower ($\text{NPP}_{\text{luc}} > \text{HANPP}_{\text{harv}}$) land use
474 efficiency would provide scientific instruction for precise agriculture.

475 In this study, although we made full use of Google Earth Engine Platform for the
476 long time series image collection and preprocessing, the STNLFFM method was time-
477 consuming, especially in the larger region. We did not test the STNLFFM-based
478 HANPP simulation in a large region (e.g., a province). Therefore, these kinds of
479 research should be enriched in the future.

480 **Conclusion**

481 In this study, the STNLFFM was applied to generate time series images with a
482 high spatial resolution. These time series images were further used to calculate the
483 HANPP in Xiong'an New Area from 2000 to 2018. Validated by multiple indicators,
484 the improved results contributed to the analysis of the spatial pattern and trend of the
485 HANPP in Xiong'an New area, from which, we concluded that the whole area had the

486 HANPP level higher than $680 \text{ g}\cdot\text{C}/\text{m}^2$. However, some built-up and water areas hold a
487 relatively low HANPP of less than $500 \text{ g}\cdot\text{C}/\text{m}^2$.

488 Most of the regions showed an increasing trend with a magnitude of less than 22
489 $\text{g}\cdot\text{C}/(\text{m}^2\cdot\text{year})$, while the southeastern area and some discrete western areas exhibited a
490 decreasing trend. The trend in the northeastern and south areas expressed a very
491 significant level ($P < 0.01$) and a significant level ($P < 0.05$) in the middle and
492 northwestern regions.

493 By discussing the correlation between natural, social, economic factors and
494 HANPP, we found that the correlation between the HANPP and the temperature had a
495 low value (-0.39 – 0.39) with non-significant level ($P > 0.1$) that occurred across the
496 whole Xiong'an New Area. Meanwhile, the HANPP responded to precipitation with a
497 correlation coefficient above 0.46 and a significant level of $P < 0.05$ in most cropland
498 regions. Fertilizer use could prompt both $\text{HANPP}_{\text{harv}}$ and HANPP to some extent. Both
499 the per capita GDP and the fraction of the non-agricultural population had a high impact
500 on $\text{HANPP}_{\text{harv}}$ with R^2 equal to 0.76 and 0.86. However, the construction and
501 development of Xiong'an New Area do not go against its sustainable development.

502 **Abbreviations**

503 NPP: Net primary production; HANPP: Human appropriation of net primary
504 production; STNLFFM: Spatial and temporal nonlocal filter-based fusion model;
505 CASA: Carnegie–Ames–Stanford approach; M–K: Mann–Kendall trend analysis
506 approach; NDVI: Normalized Difference Vegetation Index; BTH: Beijing, Tianjin, and
507 Hebei; NPP_{pot} , NPP_{act} , $\text{HANPP}_{\text{harv}}$: potential, actual and harvested NPPs, respectively.

508 **Acknowledgments**

509 We greatly appreciate the valuable comments from editor and reviewers that helped us
510 to improve the quality of this paper.

511 **Authors' contributions**

512 Jia Tang makes substantial contributions to data acquisition, processing and analysis as
513 well as drafting and critically revising of the manuscript. Qianfeng Wang contributes to
514 the development of ideas and experimental instruction as well as revision of all stages
515 and takes intellectual responsibility for its content. Other authors participate in data
516 processing and technical support of the manuscript.

517 **Funding**

518 This research received financial support from the National Natural Science Foundation
519 of China (No. 41601562) and China Scholarship Council.

520 **Availability of data and materials**

521 Both the original data and processed data are available upon request. All methods/or
522 models used herein can be obtained by contacting the corresponding author.

523 **Ethics approval and consent to participate**

524 Not applicable.

525 **Consent for publication**

526 Not applicable.

527 **Competing interests**

528 The authors declare that they have no competing interests.

529 **Authors' information**

530 ¹ Fujian Provincial Key Laboratory of Remote Sensing of Soil Erosion and Disaster Protection/College
531 of Environment and Resources, Fuzhou University, Fuzhou 350116, China
532 ² State Key Laboratory of Remote Sensing Science, Aerospace Information Research Institute, Chinese
533 Academy of Sciences, Beijing 100094, China
534 ³ Joint Global Change Research Institute, University of Maryland, College Park, MD 20740, USA

535 **Reference**

- 536 Andersen C, Donovan R, Quinn J (2015) Human Appropriation of Net Primary Production (HANPP) in
537 an Agriculturally-Dominated Watershed, Southeastern USA. *Land* 4: 513-40
- 538 Artacho P, Bonomelli C (2017) Net primary productivity and allocation to fine-root production in field-
539 grown sweet cherry trees under different soil nitrogen regimes. *Sci. Hortic.* 219: 207-15
- 540 Bishop JDK, Amaratunga GAJ, Rodriguez C (2010) Quantifying the limits of HANPP and carbon
541 emissions which prolong total species well-being. *Environ. Dev. Sustain.* 12: 213-31
- 542 Burn DH, Elnur MAH (2002) Detection of hydrologic trends and variability. *J. Hydrol.* 255: 107-22
- 543 Chen A, Li R, Wang H, He B (2015) Quantitative assessment of human appropriation of aboveground
544 net primary production in China. *Ecol Modell* 312: 54-60
- 545 Cheng Q, Liu H, Shen H, Wu P, Zhang L (2017) A Spatial and Temporal Nonlocal Filter-Based Data
546 Fusion Method. *IEEE Trans Geosci Remote Sens* 55: 4476-88
- 547 Ellis EC (2011) Anthropogenic transformation of the terrestrial biosphere. *Philos. Trans. Royal Soc. A*
548 369: 1010-35
- 549 Erb KH (2012) How a socio-ecological metabolism approach can help to advance our understanding of
550 changes in land-use intensity. *Ecological Economics* 76: 8-14
- 551 Erb KH, Haberl H, Jepsen MR, Kuemmerle T, Lindner M, Muller D, Verburg PH, Reenberg A (2013) A
552 conceptual framework for analysing and measuring land-use intensity. *Curr Opin Environ Sustain*
553 5: 464-70
- 554 Fetzel T, Gradwohl M, Erb KH (2014) Conversion, intensification, and abandonment: A human
555 appropriation of net primary production approach to analyze historic land-use dynamics in New
556 Zealand 1860-2005. *Ecological Economics* 97: 201-8
- 557 Fetzel T, Niedertscheider M, Haberl H, Krausmann F, Erb KH (2016) Patterns and changes of land use
558 and land-use efficiency in Africa 1980-2005: an analysis based on the human appropriation of net
559 primary production framework. *Regional Environmental Change* 16: 1507-20
- 560 Godfray HCJ, Beddington JR, Crute IR, Haddad L, Lawrence D, Muir JF, Pretty J, Robinson S, Thomas
561 SM, Toulmin C (2010) Food Security: The Challenge of Feeding 9 Billion People. *Science* 327:
562 812-8
- 563 Ha W, Gowda PH, Howell TA (2012) A review of downscaling methods for remote sensing-based
564 irrigation management: part I. *Irrig Sci* 31: 831-50
- 565 Haberl H (1997) Human Appropriation of Net Primary Production as an Environmental Indicator:
566 Implications for Sustainable Development. *Ambio* 26: 143-6
- 567 Haberl H, Erb KH, Krausmann F (2014) Human Appropriation of Net Primary Production: Patterns,
568 Trends, and Planetary Boundaries. *Annu Rev Environ Resour* 39: 363-91
- 569 Haberl H, Erb KH, Krausmann F, Gaube V, Bondeau A, Plutzer C, Gingrich S, Lucht W, Fischer-
570 Kowalski M (2007) Quantifying and mapping the human appropriation of net primary production
571 in earth's terrestrial ecosystems. *PNAS* 104: 12942-5
- 572 Haberl H, Erb KH, Krausmann F, Loibl W, Schulz N, Weisz H (2001) Changes in ecosystem processes
573 induced by land use: Human appropriation of aboveground NPP and its influence on standing crop
574 in Austria. *Global Biogeochem Cycles* 15: 929-42
- 575 Haberl H, Schulz NB, Plutzer C, Erb KH, Krausmann F, Loibl W, Moser D, Sauberer N, Weisz H,
576 Zechmeister HG, Zulka P (2004) Human appropriation of net primary production and species
577 diversity in agricultural landscapes. *Agric Ecosyst Environ* 102: 213-8

578 Hua X (2009) Quantifying the Human Appropriation of Net Primary Production and analysis of its multi-
579 year changes in Guangdong. Sun Yat-sen University.

580 Huang Q, Zhang FY, Zhang Q, Ou H, Jin YX (2020) Quantitative Assessment of the Impact of Human
581 Activities on Terrestrial Net Primary Productivity in the Yangtze River Delta. *Sustainability* 12: 16

582 Huang X, Luo G, Han Q (2018) Temporospatial patterns of human appropriation of net primary
583 production in Central Asia grasslands. *Ecol. Indic.* 91: 555-61

584 Huang Y, Zhang W, Sun W, Zheng X (2007) NET PRIMARY PRODUCTION OF CHINESE
585 CROPLANDS FROM 1950 TO 1999. *Ecological Applications* 17: 692-701

586 Kastner T (2009) Trajectories in human domination of ecosystems: Human appropriation of net primary
587 production in the Philippines during the 20th century. *Ecological Economics* 69: 260-9

588 Kohlheb N, Krausmann F (2009) Land use change, biomass production and HANPP: The case of
589 Hungary 1961-2005. *Ecological Economics* 69: 292-300

590 Krausmann F, Erb K-H, Gingrich S, Haberl H (2013) Global human appropriation of net primary
591 production doubled in the 20th century. *PNAS* 110: 10324-9

592 Krausmann F, Gingrich S, Haberl H, Erb KH, Musel A, Kastner T, Kohlheb N, Niedertscheider M,
593 Schwarzlmuller E (2012) Long-term trajectories of the human appropriation of net primary
594 production: Lessons from six national case studies. *Ecological Economics* 77: 129-38

595 Li F, Meng J (2018) Temporal and Spatial Variation of Human Appropriation of Net Primary Productivity
596 in the Middle Reaches of the Heihe River Basin. *ARID ZONE RESEARCH* 35: 743-52

597 Liao CH, Wang JF, Dong TF, Shang JL, Liu JG, Song Y (2019) Using spatio-temporal fusion of Landsat-
598 8 and MODIS data to derive phenology, biomass and yield estimates for corn and soybean. *Sci.*
599 *Total Environ.* 650: 1707-21

600 Lieth H. 1975. *Modeling the Primary Productivity of the World*: Springer Berlin Heidelberg.

601 M. VP, R. EP, H. EA, A. MP (1986) Human Appropriation of the Products of Photosynthesis. *BioScience*
602 6: 6

603 Mann HB (1945) NONPARAMETRIC TESTS AGAINST TREND. *Econometrica* 13: 245-59

604 Musel A (2009) Human appropriation of net primary production in the United Kingdom, 1800-2000
605 Changes in society's impact on ecological energy flows during the agrarian-industrial transition.
606 *Ecological Economics* 69: 270-81

607 Nduati E, Sofue Y, Matniyaz A, Park JG, Yang W, Kondoh A (2019) Cropland Mapping Using Fusion of
608 Multi-Sensor Data in a Complex Urban/Peri-Urban Area. *Remote Sensing* 11: 24

609 Niedertscheider M, Erb K (2014) Land system change in Italy from 1884 to 2007: Analysing the North-
610 South divergence on the basis of an integrated indicator framework. *Land Use Policy* 39: 366-75

611 Niedertscheider M, Gingrich S, Erb KH (2012) Changes in land use in South Africa between 1961 and
612 2006: an integrated socio-ecological analysis based on the human appropriation of net primary
613 production framework. *Regional Environmental Change* 12: 715-27

614 Niedertscheider M, Kuemmerle T, Muller D, Erb KH (2014) Exploring the effects of drastic institutional
615 and socio-economic changes on land system dynamics in Germany between 1883 and 2007. *Global*
616 *Environmental Change-Human and Policy Dimensions* 28: 98-108

617 Niedertscheider M, Tasser E, Patek M, Rudisser J, Tappeiner U, Erb KH (2017) Influence of Land-Use
618 Intensification on Vegetation C-Stocks in an Alpine Valley from 1865 to 2003. *Ecosystems* 20:
619 1391-406

620 O'Neill DW, Tyedmers PH, Beazley KF (2007) Human appropriation of net primary production (HANPP)
621 in Nova Scotia, Canada. *Regional Environmental Change* 7: 1-14

622 Pachavo G, Murwira A (2014) Remote sensing net primary productivity (NPP) estimation with the aid
623 of GIS modelled shortwave radiation (SWR) in a Southern African Savanna. *Int J Appl Earth Obs*
624 *Geoinf* 30: 217-26

625 Plutzer C, Kroisleitner C, Haberl H, Fetzel T, Bulgheroni C, Beringer T, Hostert P, Kastner T, Kuemmerle
626 T, Lauk C, Levers C, Lindner M, Moser D, Muller D, Niedertscheider M, Paracchini M, Schaphoff
627 S, Verburg PH, Verkerk PJ, Erb KH (2016) Changes in the spatial patterns of human appropriation
628 of net primary production (HANPP) in Europe 1990-2006. *Regional Environmental Change* 16:
629 1225-38

630 Roy DP, Kovalsky V, Zhang HK, Vermote EF, Yan L, Kumar SS, Egorov A (2016) Characterization of
631 Landsat-7 to Landsat-8 reflective wavelength and normalized difference vegetation index
632 continuity. *Remote Sens Environ* 185: 57-70

633 Running SW (2012) A Measurable Planetary Boundary for the Biosphere. *Science* 337: 1458-9

634 Schmidt M, Lucas R, Bunting P, Verbesselt J, Armston J (2015) Multi-resolution time series imagery for
635 forest disturbance and regrowth monitoring in Queensland, Australia. *Remote Sens Environ* 158:
636 156-68

637 Schwarzmuller E (2009) Human appropriation of aboveground net primary production in Spain, 1955-
638 2003: An empirical analysis of the industrialization of land use. *Ecological Economics* 69: 282-91

639 Sen, Kumar P (1968) Estimates of the Regression Coefficient Based on Kendall's Tau. *Publications of*
640 *the American Statistical Association* 63: 1379-89

641 Song CQ, Ke LH, Pan H, Zhan SN, Li K, Ma RH (2018) Long-term surface water changes and driving
642 cause in Xiong'an, China: from dense Landsat time series images and synthetic analysis. *Science*
643 *Bulletin* 63: 708-16

644 Tang J, Zeng J, Zhang L, Zhang R, Li J, Li X, Zou J, Zeng Y, Xu Z, Wang Q, Zhang Q (2020a) A modified
645 flexible spatiotemporal data fusion model. *Front Earth Sci* doi: 10.1007/s11707-019-0800-x

646 Tang J, Zeng J, Zhang Q, Zhang R, Leng S, Zeng Y, Shui W, Xu Z, Wang Q (2020b) Self-adapting
647 extraction of cropland phenological transitions of rotation agroecosystems using dynamically fused
648 NDVI images. *Int J Biometeorol* 4: 1-11

649 Wang HB, Li X, Ma MG, Geng LY (2019) Improving Estimation of Gross Primary Production in Dryland
650 Ecosystems by a Model-Data Fusion Approach. *Remote Sensing* 11: 22

651 Wang PJ, Wu DR, Yang JY, Ma YP, Feng R, Huo ZG (2020) Summer maize growth under different
652 precipitation years in the Huang-Huai-Hai Plain of China. *Agric For Meteorol* 285: 12

653 Wang Q, Wu J, Li X, Zhou H, Yang J, Geng G, An X, Liu L, Tang Z (2017a) A comprehensively
654 quantitative method of evaluating the impact of drought on crop yield using daily multi-scale SPEI
655 and crop growth process model. *Int J Biometeorol* 61: 685-99

656 Wang QF, Zeng JY, Leng S, Fan BX, Tang J, Jiang C, Huang Y, Zhang Q, Qu YP, Wang WL, Shui W
657 (2018) The effects of air temperature and precipitation on the net primary productivity in China
658 during the early 21st century. *Front Earth Sci* 12: 818-33

659 Wang SS, Mo XG, Liu ZJ, Baig MHA, Chi WF (2017b) Understanding long-term (1982-2013) patterns
660 and trends in winter wheat spring green-up date over the North China Plain. *Int J Appl Earth Obs*
661 *Geoinf* 57: 235-44

662 Wang XY, Xue S, Xie GH (2012) Value-taking for residue factor as a parameter to assess the field residue
663 of field crops. *Journal of China Agricultural University*

664 Warman RD (2014) Global wood production from natural forests has peaked. *Biodivers. Conserv.* 23:
665 1063-78

666 Xie G, Han D, Wang X, Lu R (2011) Harvest index and residue factor of cereal crops in China. *Journal*
667 *of China Agricultural University* 16: 1-8

668 Xie SL, Su YB, Xu WH, Cai WB, Wang XK, Lu F, Ouyang ZY (2019) The effect of habitat changes
669 along the urbanization gradient for breeding birds: an example from the Xiong'an New Area. *Peerj*
670 7: 22

671 Xu CL, Tao HB, Tian BJ, Gao YB, Ren JH, Wang P (2016) Limited-irrigation improves water use
672 efficiency and soil reservoir capacity through regulating root and canopy growth of winter wheat.
673 *Field Crops Res.* 196: 268-75

674 Xu F, Yang ZF, Chen B, Zhao YW (2013) Impact of submerged plants on ecosystem health of the plant-
675 dominated Baiyangdian Lake, China. *Ecol Modell* 252: 167-75

676 Xu HQ, Shi TT, Wang MY, Fang CY, Lin ZL (2018) Predicting effect of forthcoming population growth-
677 induced impervious surface increase on regional thermal environment: Xiong'an New Area, North
678 China. *Build Environ* 136: 98-106

679 Xu ZX, Chen YN, Li JY (2004) Impact of climate change on water resources in the Tarim River basin.
680 *Water Resour. Manag.* 18: 439-58

681 Zhang FY, Pu LJ, Huang Q (2015) Quantitative Assessment of the Human Appropriation of Net Primary
682 Production (HANPP) in the Coastal Areas of Jiangsu, China. *Sustainability* 7: 15857-70

683 Zhang Y, Pan Y, Zhang X, Wu J, Yu C, Li M, Wu J (2018) Patterns and dynamics of the human
684 appropriation of net primary production and its components in Tibet. *J. Environ. Manage.* 210: 280-
685 9

686 Zhao N, Yue TX, Li H, Zhang LL, Yin XZ, Liu Y (2018) Spatio-temporal changes in precipitation over
687 Beijing-Tianjin-Hebei region, China. *Atmos Res* 202: 156-68

688 Zhou C, Elshkaki A, Graedel TE (2018) Global Human Appropriation of Net Primary Production and
689 Associated Resource Decoupling: 2010-2050. *Environ. Sci. Technol.* 52: 1208-15

690 Zhou Q, Zhao X, Wu DH, Tang RY, Du XZ, Wang HY, Zhao JC, Xu PP, Peng YF (2019) Impact of
691 Urbanization and Climate on Vegetation Coverage in the Beijing-Tianjin-Hebei Region of China.
692 *Remote Sensing* 11: 16

693 Zhu W, Pan Y, Zhang J (2007) ESTIMATION OF NET PRIMARY PRODUCTIVITY OF CHINESE
694 TERRESTRIAL VEGETATION BASED ON REMOTE SENSING. *J Plant Ecol* 31: 413-24

695 Zhu X, Chen J, Gao F, Chen X, Masek JG (2010) An enhanced spatial and temporal adaptive reflectance
696 fusion model for complex heterogeneous regions. *Remote Sens Environ* 114: 2610-23

697 Zhu X, Helmer EH, Gao F, Liu D, Chen J, Lefsky MA (2016) A flexible spatiotemporal method for fusing
698 satellite images with different resolutions. *Remote Sens Environ* 172: 165-77

699

700